Ocean Systems Engineering, *Vol. 12, No. 2 (2022) 247-265*
https://doi.org/10.12989/ose.2022.12.2.247

CFD simulations of a performance-scaled wind turbine

Maokun Ye*[1], Hamn-Ching Chen[1,2a] and Arjen Koop[3]

[1]*Department of Ocean Engineering, Texas A&M University, College Station, Texas, USA*
[2]*Zachry Department of Civil & Environmental Engineering, Texas A&M University, College Station, Texas, USA*
[3]*MARIN – Maritime Research Institute Netherlands, Wageningen, The Netherlands*

(Received April 6, 2022, Revised May 26, 2022, Accepted June 3, 2022)

Abstract. In the present study, we focus on the CFD simulations for the performance and the rotor-generated wake of a model-scale wind turbine which was designed for wave tank experiments. The CFD simulations with fully resolved rotor geometry are performed using MARIN's community-based open-source CFD code ReFRESCO. The absolute formulation method (AFM) is leveraged to model the rotating wind turbine. The $k-\omega$ SST turbulence model is adopted in the incompressible Reynolds Averaged Navier-Stokes (RANS) simulations. First, the thrust and torque coefficients, C_T and C_P, are calculated at different Tip Speed Ratios (TSR), and the results are compared against the experimental data and previous numerical results. The pressure distribution of the turbine blades at the 70% span is obtained and compared to the results obtained by other tools. Then, a verification study aiming at quantifying the discretization uncertainty of the turbine performance with respect to the grid resolution in the wake region is performed. Last, the rotor-generated wake at the TSR of 7 is presented and discussed.

Keywords: CFD simulation; FOWT; numerical uncertainties; wind turbine

1. Introduction

To achieve the goal of carbon neutrality in the coming decades, electricity generation from renewable sources, including wind, will need a severalfold increase (Veers *et al*. 2019). More wind farms need to be deployed both onshore and offshore. Offshore wind energy is rapidly maturing and has the potential to play a significant role in the future energy system (IEA 2019). In particular, the floating offshore wind turbine (FOWT) has been an attractive concept due to its capability of deployment in deepwater regions where higher wind speeds exist. Especially in the U.S., about 60% of the offshore wind resources are in areas where the water is so deep that fixed foundations are not practical (Wind Energy Technologies Office 2021). Therefore, the development of FOWT is of importance to the renewable energy transition. To be competitive in the future energy market, the Levelized cost of energy (LCOE) of floating offshore wind farms needs to be as low as possible, hence accurate power predictions for floating wind farms are crucial. However, this task is even more challenging than onshore ones because the floating platforms will have a six-degrees-of-

*Corresponding author, Ph.D. Student, E-mail: leafsunny@tamu.edu
[a]A.P. & Florence Wiley Professor I

http://www.techno-press.org/?journal=ose&subpage=7 ISSN: 2093-6702 (Print), 2093-677X (Online)

freedom motion due to the combined effect of ocean waves, current, and mooring lines (Wang *et al*. 2021).

In the last two decades, computational fluid dynamics (CFD) methods with different levels of complexity and accuracy have been extensively used in the predictions of wind turbine performance and wakes. One commonly used approach to calculating the flow around and behind a wind turbine is to couple the RANS or LES solvers with Blade element method (BEM) based methods. In these calculations, the influences of wind turbines are modeled as forces in the fluid field, thus the need of resolving the geometry of the blades and the fluid boundary layers is circumvented (Troldborg 2009). This approach is particularly popular in wind turbine wake simulations, examples can be found in Troldborg (2009), Wu and Porté-Agel (2015), and Xie and Archer (2017). The adoption of these approaches is often inevitable when it comes to calculations of wind turbine wakes because it is extremely resource-demanding to resolve both the turbine boundary layers and the wake regions at the same time.

However, those methods may be questioned as they usually assume that the flow on the surface of the blades is 2 dimensional and this may not be physically correct in the real world (Duque 1999), especially for FOWTs of which rotor diameters are generally larger than those of onshore wind turbines (Office of Energy Efficiency & Renewable Energy 2021). In addition, unique challenges arise from the six-degrees-of-freedom platform motion, as mentioned earlier. In some situations, e.g., platform surge, the wind turbine blades will interact with their own wake (Tran and Kim 2016). According to the above discussions, the simplification of the boundary layers of the wind turbines in the CFD simulations may result in large uncertainties in the predictions of the performance of FOWTs, thus undermining the credibility of the predictions of the overall wind farm power production. As a result, CFD simulations including fully resolved wind turbine geometries may provide more accurate results.

In recent years, thanks to the continual decrease in computational cost, CFD simulations with fully resolved rotor geometries are becoming increasingly popular in wind turbine simulations. Li *et al.* (2012) performed CFD simulations for the NREL phase VI wind turbine by leveraging the dynamic overset technique. In the study, the geometries of the turbine including the tower are resolved. Both the unsteady RANS and the detached eddy simulation (DES) approaches were used in the simulations. Lynch and Smith (2013) also investigated the NREL phase VI turbine by using the CFD code FUN3D with unstructured overset grids. Tran and Kim (2016) studied the performance of the NREL 5 MW turbine under prescribed platform motions by using Star-CCM+. In the study, RANS equations with the $k-\omega$ SST turbulence model are solved, and the overset grid technique is adopted.

While the above simulations all adopted an unsteady-state framework, steady-state CFD simulations of wind turbines can be legitimately performed in cases where the tower effect may not be significant (Ye *et al.* 2022). One major advantage of this approach is that the computational resource required is significantly lower than the resource needed in unsteady CFD simulations. Mike and Vaz (2015) performed steady simulations using the CFD code ReFRESCO, and the effects of the domain size, grid resolutions, and turbulence models on the CFD predictions were evaluated. Ye *et al.* (2021) performed CFD simulations with fully resolved rotor geometry for two tandemly arrayed wind turbines, in which steady-state RANS simulations were carried out by using the absolute formulation method (AFM). Ye *et al.* (2022) compared the results of the Norwegian University of Science and Technology (NTNU) Blind Test (BT) 1 wind turbine obtained from steady and unsteady CFD simulations. They found that the C_T and C_P of the turbine from different approaches were very similar, while the asymmetric profiles of the wake could not be captured due

to the neglect of the tower structure in the steady calculations.

Aiming at the aerodynamics of FOWT, the main target of the present work is to calculate the performance and the wake of a model-scale three-bladed wind turbine which was designed for wave tank experiments (de Ridder *et al.* 2014). RANS equations combined with the $k-\omega$ SST turbulence model are solved in a steady-state framework. The rotor geometries including the blades, hub, and nacelle are fully resolved in the simulations. In addition to the flow around the rotor, the wake regions including the near wake and far wake are also resolved in the simulations.

The paper is organized as follows. The numerical methods including the wind turbine geometry, the mesh generation, and the CFD approach are described first. Then, the CFD results of the turbine's performance and the pressure distribution of the blades at the 70% span are obtained and compared against the experimental data and previous studies. Flow near the turbine blades and the pressure distribution over the blade surface are visualized and discussed. Afterward, a verification study aiming at quantifying the discretization uncertainty of the turbine performance with respect to the grid resolution of the wake region is performed. Further, the wake characteristics of the turbine at the TSR value of 7 are presented and discussed. Last, conclusions are drawn from the results and discussions.

2. Numerical methods

2.1 MARIN Stock Wind Turbine (MSWT)

The turbine used in the current study is the MARIN Stock Wind Turbine (MSWT). MSWT is a model-scale wind turbine designed specifically for model-scale floating offshore wind turbine (FOWT) experiments (Make *et al*. 2015). The MSWT was designed based on the concept of "performance scaling". In wave tank experiments, the hydrodynamic responses of the model-scale FOWT can be reasonably obtained by using Froude-scaling, while the aerodynamic characteristics, i.e., C_T and C_P, of the turbine could be very different from those of full-scale ones if the same Froude-scaling was applied. As a result, the model-scale experiments of a FOWT under both wave and wind may not be able to represent the full-scale responses of that FOWT. To resolve this issue, the so-called performance-scaling method (de Ridder *et al.* 2014, Martin *et al.* 2014) is applied to the NREL 5 MW (Jonkman *et al.* 2009) baseline turbine with a scale factor of 50, such that the values of C_T and C_P of the model-scale turbine are approximately the same as those of the full-scale NREL 5 MW baseline turbine.

2.2 Computational domain

The computational domain used in this work is based on the previous study by Make and Vaz (2015). In their study, a thorough verification procedure was carried out to quantify the discretization error, and the effect of domain size was also scrutinized. There were 3 computational domains used in their simulations. The smallest domain is a cylinder that has an upstream length of 5 times turbine diameters (D), a downstream length of 20 D, and a diameter of 10 D. The height and the radius of the largest domain are 3 times as long as those of the smallest domain, i.e., the largest domain is 27 times as large as the smallest one in volume. It was found that even for the smallest domain, the value of C_P has only a negligible variation, i.e., 3%, compared to the value of the largest domain.

The value of C_T has an even smaller variation of less than 1% compared to that of the largest

one. In addition, in their study, only the performance of the wind turbine was of interest, therefore, only the boundary layers of the wind turbine were well resolved by fine computational cells while the cells in the wake region are coarse. However, in the current study, our goal is to resolve the boundary layers of the rotor and the rotor-generated wake simultaneously. Therefore, fine computational cells in the wake region are required. As a compromise between the grid resolution and the total number of cells, in the present study, the diameter of the computational domain is chosen to be 3 D, the upstream length 5 D, and the downstream length 20 D.

Further, for better control of the grid quality and density, the multi-block technique is applied to the grid generation. The entire computational domain is subdivided into 5 blocks in which computational meshes will be constructed separately. By using this approach, we can leverage different tools to generate desired grids for different blocks, and we can control the grid density of a certain block without affecting other parts. An illustration of the computational domain used in the present study and its boundary names are shown in Fig. 1.

2.3 Computational grid generation

As mentioned earlier, for better control of the grid quality, the computational grids used in the present work are generated by leveraging the multi-block technique and the sliding interface capability (MARIN 2017) of ReFRESCO. Two commercial grid generation packages are used to generate the high-quality hexahedral meshes in this work.

Hexpress (https://www.numeca.com/product/omnis-hexpress) is used for the grid generation of the disc block which contains the rotor boundary layers (as shown in Fig. 1). HEXPRESS generates unstructured mesh with pure hexahedral elements. In the mesh generation procedure, HEXPRESS will start from the largest mesh elements and then halve them several times near the turbine surface until the refined mesh elements can adequately capture the geometry. Boundary layers are inserted in the last step with the criterion of $y^+ < 1$, and the cell expansion ratio normal to the wall is 1.2. Due to its fully automated procedure, this tool is fast and effective for the mesh generation of near-surface regions where high skews of the geometry exist. An illustration of the computational cells near the blade is shown in Fig. 2.

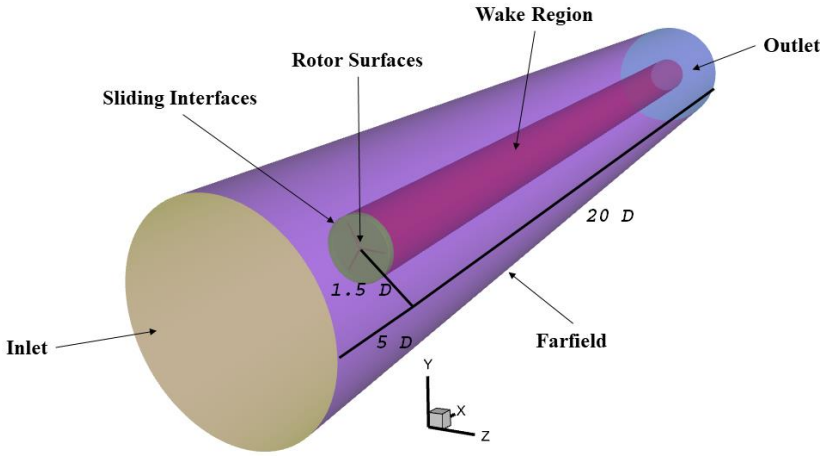

Fig. 1 Computational domain

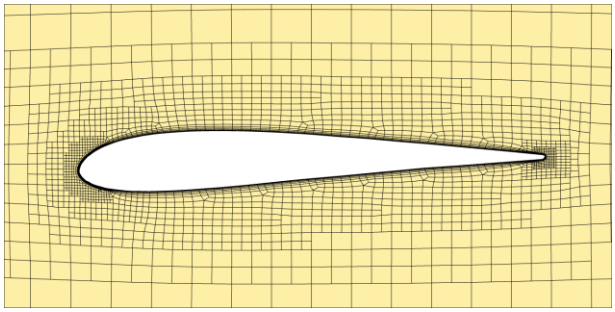

Fig. 2 Computational cells near the blade

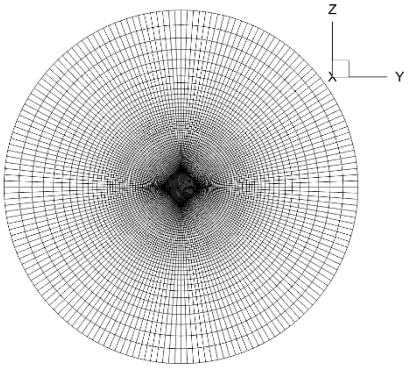

Fig. 3 Cross-section of the wake region mesh

For the grid generation of the other blocks, high-quality structured meshes are constructed by using PointWise (https://www.pointwise.com). The cross-section view of the computational grids generated for the wake regions are shown in Fig. 3.

2.4 CFD approach

2.4.1 Flow solver

MARIN's community-based open-source CFD code ReFRESCO (www.refresco.org) is adopted in the present work as the unsteady viscous flow solver. ReFRESCO solves multiphase incompressible Reynolds-Averaged Navier-Stokes (RANS) equations by using the finite-volume method with cell-centered variables. Turbulence models including RANS, Partially-Averaged Navier-Stokes (PANS), Large Eddy Simulation (LES), and Detached Eddy Simulation (DES) can be selected in ReFRESCO and the code can run in parallel on HPC clusters.

2.4.2 Governing equations

In the present work, the incompressible RANS equations combined with the $k-\omega$ SST (Menter *et al*. 2003) turbulence model are solved. In the steady-state calculations, the Absolute-Formulation Method (AFM) is used. The turbine rotation is modeled by conceptually rotating the entire flow field. In these simulations, the RANS equations are solved in the moving reference frame but written in terms of inertial reference frame quantities, and are given as

$$\int_{\mathcal{S}} \left(\vec{V} - \overrightarrow{V_g}\right) \cdot \vec{n}\, d\mathcal{S} = 0 \tag{1}$$

$$\begin{aligned} &\int_{\mathcal{S}} \left[\rho\vec{V}\left(\vec{V} - \overrightarrow{V_g}\right) \cdot \vec{n}\right] d\mathcal{S} \\ &= \int_{\mathcal{S}} (\mu + \mu_T)\left[\left(\nabla\vec{V} + \nabla\vec{V}^T\right)\right] \cdot \vec{n} d\mathcal{S} - \int_{\mathcal{V}} \nabla\left(p + \frac{2}{3}\rho k\right) d\mathcal{V} \\ &- \int_{\mathcal{V}} \rho\left(\overrightarrow{\Omega} \times \vec{V}\right) d\mathcal{V} + \int_{\mathcal{V}} \rho\vec{B}\, d\mathcal{V} \end{aligned} \tag{2}$$

Here, ρ is the density of the fluid, $\vec{V}$ is the velocity vector of the fluid field, $\vec{n}$ is the unit normal vector of the surfaces of the control volume, $\vec{B}$ is the body force vector, and $\overrightarrow{V_g}$ stands for the motion of the grid.

2.4.3 Numerical settings

Steady-state calculations are performed in the present study. The momentum and turbulence equations are discretized by using the HARMONIC scheme (van Leer 1974), and the FRESCO (Klaij *et al*. 2018) algorithm is used for the mass-momentum coupling. A uniform inflow velocity of 2 *m/s* and a turbulence intensity level of 10 % are specified at the inlet boundary for all simulations. Different TSR values are achieved by changing the rotating speed of the turbine. The zero gradient condition is defined at the outlet boundary, and the fixed pressure boundary condition is applied to the Farfield (see Fig. 1) boundary. The interfaces between the different mesh blocks are set as BCInterface in ReFRESCO, which allows the flow information to be transferred from one to another. Last, the no-slip condition is applied to all the wall boundaries including the blades, hub, and nacelle. The Reynolds number used in the present study is calculated at 70 % of the blade span. As the result, the chord-based Reynolds number at TSR of 7 is approximately 6×10^4.

3. Numerical results

The numerical results in this study are presented in two parts separately, i.e., the performance, C_T and C_P, and the wake of the MSWT. The grid resolutions needed to accurately predict the performance and the wake of a wind turbine are very different. For the values of C_T and C_P, only fine resolution of the grids around the wind turbine is required (Ye *et al.* 2022), while the resolution in the wake region can be relatively coarse. However, if the wake characteristics are also of interest, fine resolution of the grids in the wake region is inevitable, and the computational resource needed will rise accordingly.

3.1 Performance of the MSWT at different TSRs

The values of C_T and C_P for tip-speed ratios (TSR) of 3, 5, 7, and 9 are computed first. The near-rotor grid resolution is chosen based on previous studies (Ye *et al.* 2021). Note that a thorough verification and validation (V & V) study for the performance of the same turbine using ReFRESCO has been performed by Mike and Vaz (2015). Therefore, the verification study for the predictions of

C_T and C_P with respect to the grid resolution in the near-rotor regions is neglected in the current study.

The results are compared with MARIN's model-scale experiments and previous numerical studies directly, as shown in Fig. 4. For both C_T and C_P, the results are in good agreement with both the experimental data and the previous numerical results. And the contours of wind velocity magnitude for TSR = 7 at the *yOz* plane is shown in Fig. 5.

Then, the pressure distribution of the blades at the 70% span is obtained and compared to a two-dimensional computational result (de Ridder *et al*. 2014), as shown in Fig. 6. In Fig. 6, the red circles are the normalized pressure values on the pressure side, and the blue ones on the suction side. It can be observed that the results obtained by ReFRESCO are in good agreement with the 2-D calculations, re-assuring the two-dimensional feature of the flow at this location.

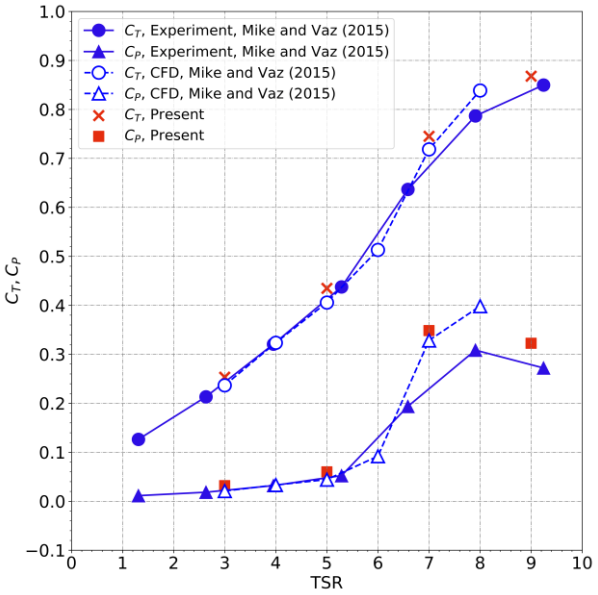

Fig. 4 Comparisons of C_T and C_P at different TSRs

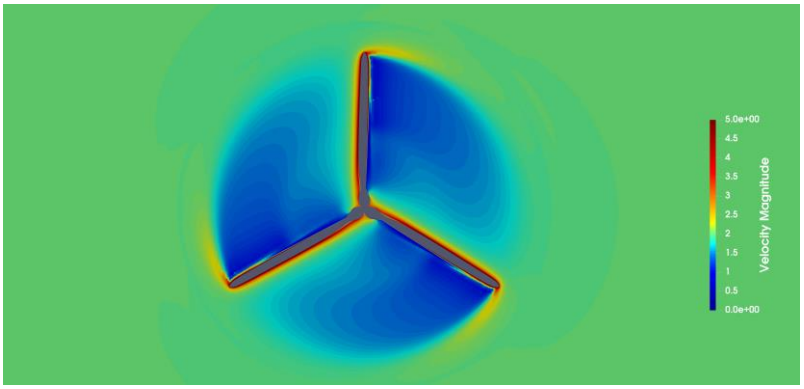

Fig. 5 Velocity magnitude at the *yOz* plane for TSR =7

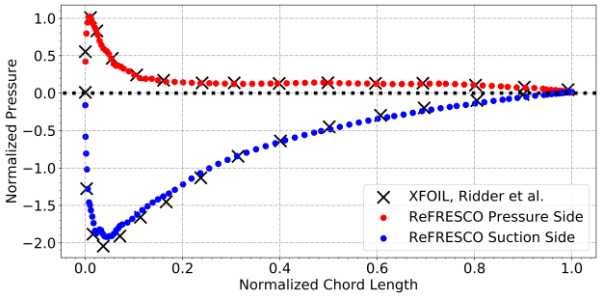

Fig. 6 Normalized pressure distribution at the 70% blade span

To better understand the flow around the turbine blades, the velocity magnitude contours and the pressure distributions around the blades at the 30% and 70% blade span are presented in Figs. 7 and 8, respectively. Note that the free-stream flow is from top to bottom in Figs. 7 and 8, and the blade cross-section is moving from right to left, as indicated in Figs. 7(a) and 8(a). Therefore, the upper side of the blade cross-section is the pressure side, and the lower the suction side.

For the velocity magnitude contours and the pressure distribution at the 30% blade span, as shown in Fig. 7, the direction of the effective velocity becomes more parallel to the rotating direction of the blades as the value of TSR increases. In other words, the angle of attack of a given blade cross-section decreases with the increase of the TSR value. As the result, it can be observed that at low TSR values of 3 and 5, obvious flow separation occurs, as shown in Figs. 7(a)-7(d), while the flow remains well attached at high TSR values, as shown in Figs. 7(e)-7(h). For the velocity magnitude contours and the pressure distribution at the 70% blade span, as shown in Fig. 8, the overall trend of the flow around the blade cross-section is similar to the trend of the 30% span. However, because the angle of attack is smaller at the 70% blade span than it at the 30% blade span, the flow separation is less severe at the 70% blade span for the TSR values of 3 and 5.

The pressure contours on the blade surface at TSR values of 3, 5, 7, and 9 are presented in Fig. 9. The figures in the left column is the pressure distribution over the pressure side and the right over the suction side. It can be observed that as the value of TSR increases from 3 to 9, the pressure at the leading edge of the pressure side increases and the pressure at the leading edge of the suction side decreases. This is an indication that the blade performance is approaching its design condition in which more lift will be produced by the blade.

3.2 Wake characteristics of MSWT

For the calculations of the wake, a verification study for the turbine performance with respect to the grid resolution of the wake region is performed first. The purpose of this verification study is to quantify the influence of the grid resolution in the wake region on the turbine performance. Four computational grids for the wake region are generated, and the basic information is summarized in Table 1. Simulation time ranges from roughly 18 to 40 hours. All simulations are performed on the Grace cluster of the TAMU HPRC by using 30 Intel Xeon 6248R (Cascade Lake) 3.0GHz 24-core processors, i.e., in total 720 cores. Illustrations of the coarsest and finest grids used in the verification study are shown in Figs. 10 and 11, respectively. It can be observed that only the wake region is refined in the study, while the other parts remain the same, as discussed in the earlier sections. By adopting this approach, we can avoid the problem that the total number of computational cells to be too large.

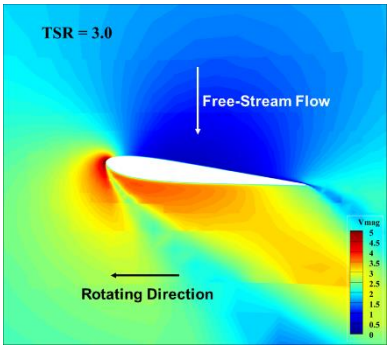

(a) Velocity magnitude contour for TSR = 3.0

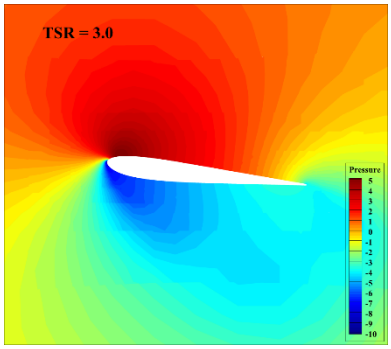

(b) Pressure distribution for TSR = 3.0

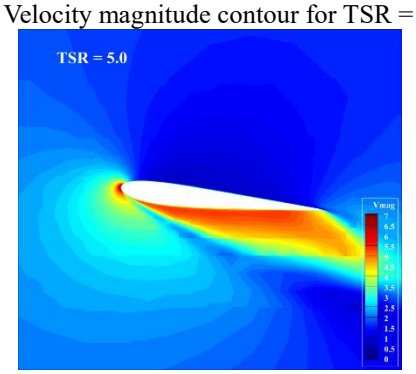

(c) Velocity magnitude contour for TSR = 5.0

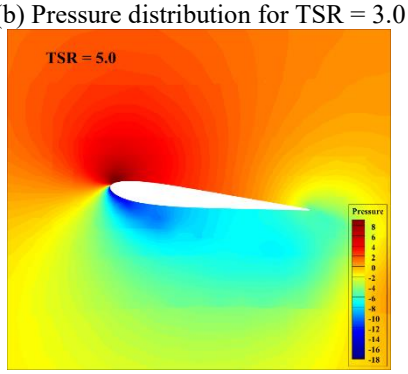

(d) Pressure distribution for TSR = 5.0

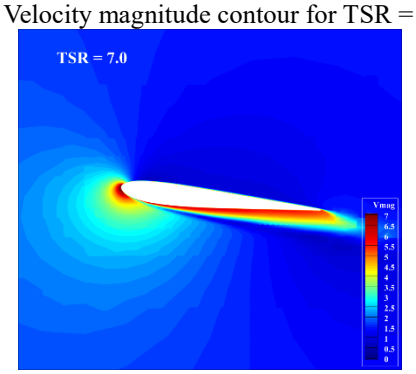

(e) Velocity magnitude contour for TSR = 7.0

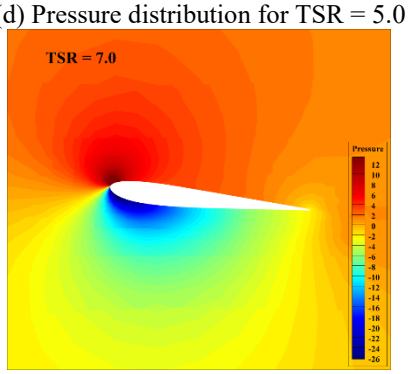

(f) Pressure distribution for TSR = 7.0

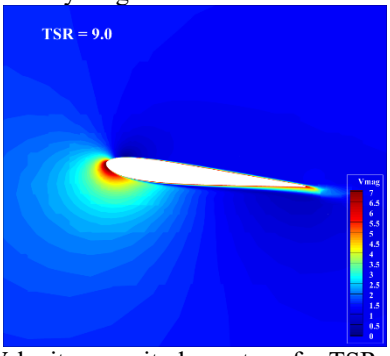

(g) Velocity magnitude contour for TSR = 9.0

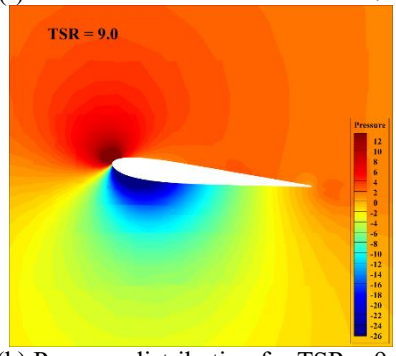

(h) Pressure distribution for TSR = 9.0

Fig. 7 Velocity magnitude contours and pressure distributions at 30% blade span for TSR values of 3.0, 5.0, 7.0, and 9.0

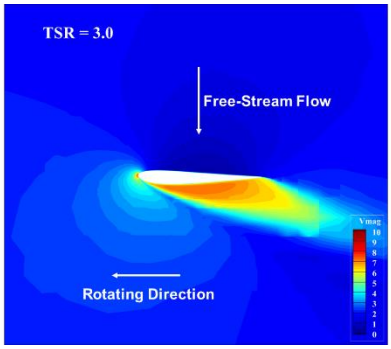

(a) Velocity magnitude contour for TSR = 3.0

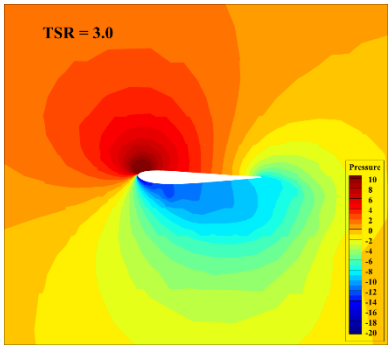

(b) Pressure distribution for TSR = 3.0

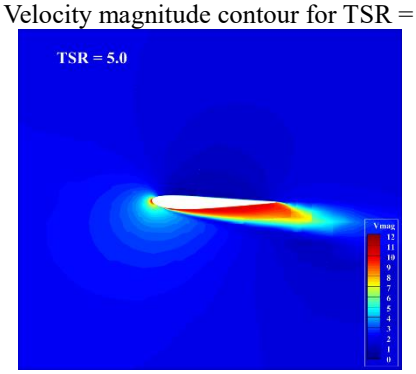

(c) Velocity magnitude contour for TSR = 5.0

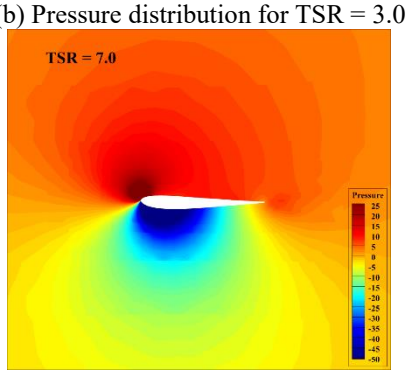

(d) Pressure distribution for TSR = 5.0

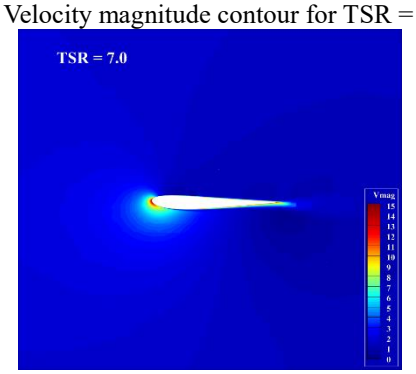

(e) Velocity magnitude contour for TSR = 7.0

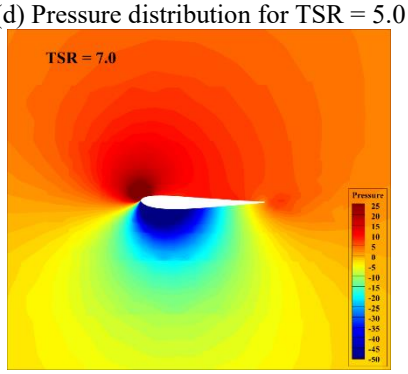

(f) Pressure distribution for TSR = 7.0

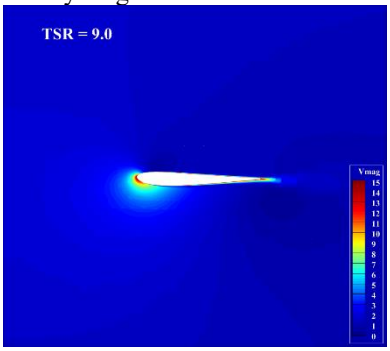

(g) Velocity magnitude contour for TSR = 9.0

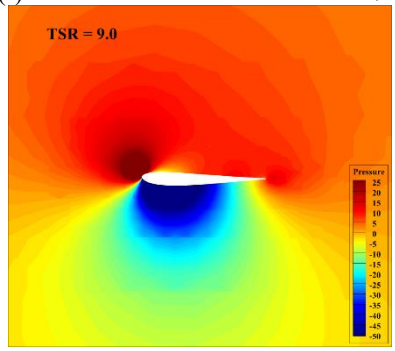

(h) Pressure distribution for TSR = 9.0

Fig. 8 Velocity magnitude contours and pressure distributions at 70% blade span for TSR values of 3.0, 5.0, 7.0, and 9.0

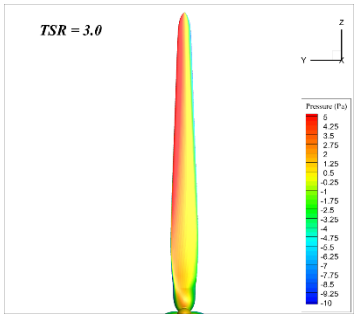

(a) Pressure distribution over the pressure side for TSR = 3.0

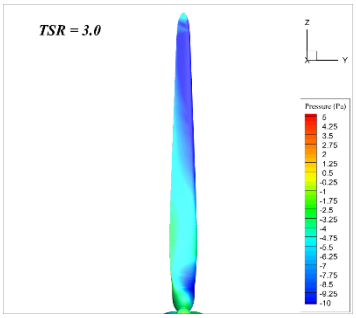

(b) Pressure distribution over the suction side for TSR = 3.0

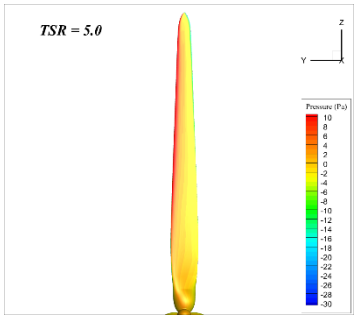

(c) Pressure distribution over the pressure side for TSR = 5.0

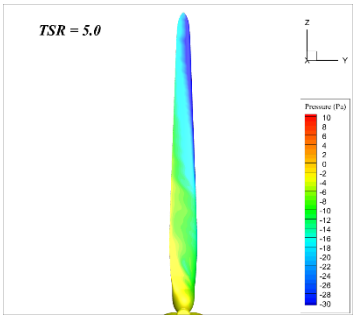

(d) Pressure distribution over the suction side for TSR = 5.0

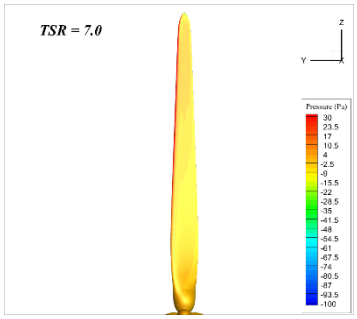

(e) Pressure distribution over the pressure side for TSR = 7.0

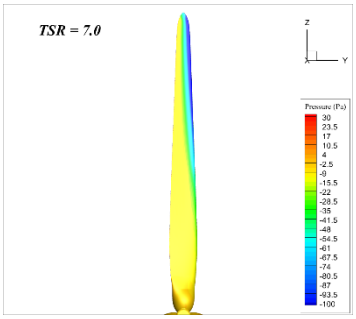

(f) Pressure distribution over the suction side for TSR = 7.0

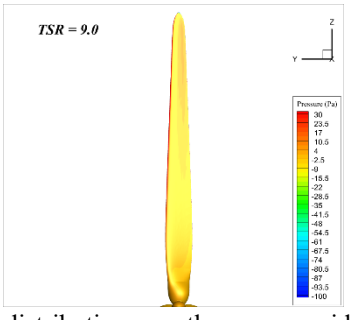

(g) Pressure distribution over the pressure side for TSR = 9.0

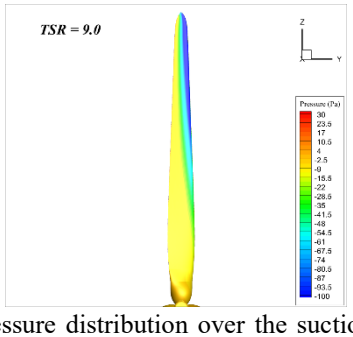

(h) Pressure distribution over the suction side for TSR = 9.0

Fig. 9 Pressure distributions over the pressure and suction sides of the blade for TSR values of 3.0, 5.0, 7.0, and 9.0

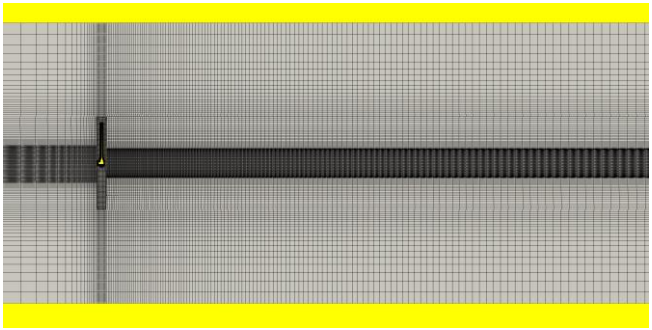

Fig. 10 Wake region girds of G4

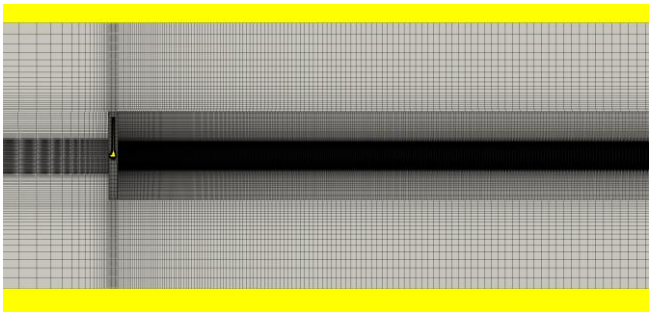

Fig. 11 Wake region girds of G1

Table 1 Computational resource summary for the grid refinement study

Grid	No. Cells in Wake Block	Total No. Cells	Total Iterations	Computational Time (hours)
G1	20,787,480	34,269,648	50,000	40.4
G2	10,440,000	23,922,168	50,000	27.8
G3	5,311,872	18,794,040	50,000	22.2
G4	2,605,000	16,087,168	50,000	18.4

3.2.1 Verification study for the turbine performance with respect to the grid resolution of the wake region

A thorough verification study has been performed on the same MSWT in a previous study (Make and Vaz 2015) with an emphasis on the grid resolution of near-rotor regions. However, when dealing with the turbine wakes, grid resolutions in both the near-rotor and the wake regions are important to the simulations, and the grid resolution in the wake region may also affect the performance of the rotor. In the present verification study, we aim at quantifying the influence of the grid resolution of the wake region on the CFD predictions of the turbine performance.

Numerical errors and uncertainties

The terms “numerical errors” and “numerical uncertainties” are closely related but conceptually different. The “error” is the difference between the simulation results and the “exact” solution,

whereas the "uncertainty" defines an interval that contains the "exact" solution with a certain degree of confidence (Roach 2009). Here, under most of the circumstances, the "exact" solution is not known and thus a procedure to get it from the available simulation results is needed.

In general, there are three types of numerical errors present in CFD calculations, which are round-off, iterative, and discretization errors (Eça and Hoekstra 2014). The round-off error ε_{ro} comes with the fact that the computers only have finite floating-point precision, but it is assumed negligible when double-precision machines are used. The iterative error ε_{it} is the consequence of iteratively solving the nonlinear governing equations, and it is also considered small when the solution is well converged. The discretization error ε_d, however, is the result of discretizing the governing partial differential equations into the algebraic equations and is considered dominant among the numerical errors in CFD simulations. The practice to quantify the numerical uncertainty related to the discretization error is called the verification procedure, in which the numerical uncertainty U_ϕ of a result ϕ_i is estimated while the exact solution ϕ_0 is unknown (Mike and Vaz, 2015).

Verification procedure

The verification procedure adopted in this study is proposed by Eça and Hoekstra (2014). For steady state simulations, the discretization error comes solely from the spatial component and thus can be expressed as

$$\varepsilon_d \simeq \delta_{RE} = \phi_i - \phi_0 = \alpha_x h_i^{p_x} \tag{3}$$

In Eq. (3), ϕ_{ij} represents any quantity obtained from the simulation using grid i. ϕ_0 denotes the "exact" solution which is obtained by fitting the data points in a certain manner. p_x is the observed order of convergence in space, and h_i is the relative grid size which is defined as:

$$h_i = \left(\frac{N_{cells_1}}{N_{cells_i}}\right)^{\frac{1}{n_d}} \tag{4}$$

In Eq. (4), N_{cells_i} denotes the number of cells in grid i for the simulation. Note that the finest grid is denoted by the subscript 1, and this implies that h_i is equal to 1 for the simulation using the finest grid spacing. n_d is equal to 3 in the three-dimensional computations.

It should be noted that in Eq. (3) there are 3 unknowns, thus at least 3 simulations with different h_i are needed to determine those unknowns. However, more simulations are recommended to perform the error estimation utilizing least-squares (Eça and Hoekstra, 2014). For the least-squares error estimation, the 3 unknowns in Eq. (3), ϕ_0, α_x, and p_x, are determined from the minimum of the following function

$$S_{RE}(\phi_0, \alpha_x, p_x) = \sqrt{\sum_{i=1}^{n_g} w_i\left[\phi_i - \left(\phi_0 + \alpha_x h_i^{p_x}\right)\right]^2} \tag{5}$$

Here, n_g is the number of grids used in the verification study. w_i represents the weight for a given solution such that the importance of different grid spacing can be distinguished, i.e., larger weights are given to solution obtained by finer of h_i. More details of this procedure can be found in Eça and Hoekstra (2014).

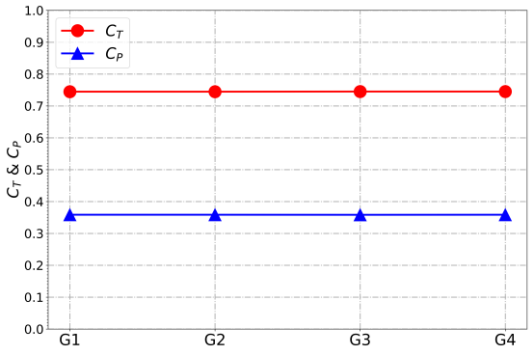

Fig. 12 C_T and C_P obtained using the four different grids

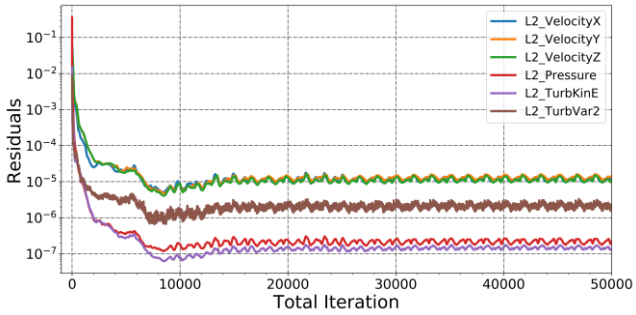

Fig. 13 Residuals for G4 case

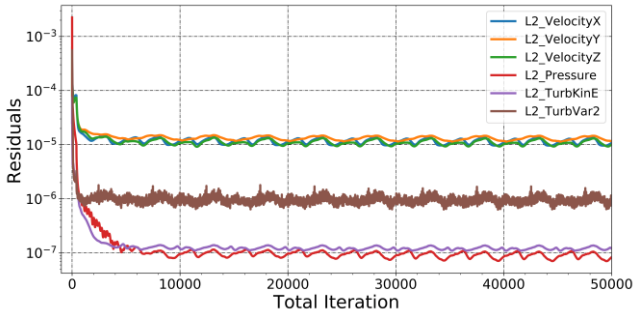

Fig. 14 Residuals for G1 case

Results of the verification study

First, the values of C_T and C_P obtained by using those 4 grids are presented in Fig. 12. It can be seen that those four results are very close to each other, indicating that the grid resolution in the wake region has a negligible influence on the turbine performance.

Then, the residuals representing the iterative convergence of the G4 and G1 simulations are shown in Figs. 13 and 14, respectively. It can be observed that the L_2-norm of the residuals for both simulations dropped to or under the level of 10^{-5} and remained smooth. This indicates that the simulations were well converged and the iterative errors ε_{it} in the simulations are small and thus can be legitimately neglected in the uncertainty estimations.

Table 2 Uncertainty estimation for C_T and C_P with respect to the different grids of wake region

Grid	h_i/h_1	C_T	$U_T^{\emptyset}$	C_P	$U_P^{\emptyset}$
	h_0	0.7470	–	0.3590	–
G1	1.00	0.7448	0.4%	0.3587	0.0%
G2	1.26	0.7447	0.5%	0.3586	0.1%
G3	1.58	0.7452	0.4%	0.3584	0.0%
G4	2.00	0.7452	0.4%	0.3586	0.1%

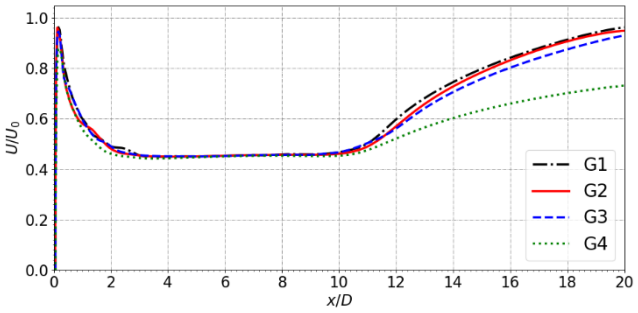

Fig. 15 Normalized center-line velocities obtained by using the four different grids

Finally, Table 2 lists the uncertainties of C_T and C_P obtained from the verification procedure by using the 4 different grids. Note that h_0 represents the extrapolated value, i.e., the "exact" value, obtained from the verification procedure. It is clear that the results obtained from the different grids are very close to each other even for the coarsest grid, and all the estimated uncertainties are below 0.5%. This result confirms that the grid resolution in the wake region does not significantly affect the performance of the rotor in the current simulations.

3.2.2 Wake characteristics of MSWT at TSR = 7

To determine the proper grid resolution in the wake region for the calculations of the wake characteristics, the normalized center-line velocities for the turbine are compared among the four different grids, as shown in Fig. 15. For each of the four grids, the center-line velocity behind the turbine remains low until about 10 D downstream, and then gradually increases and recovers to the value of inlet velocity. However, the result from the coarsest grid, G4, has a large difference compared to those from the other grids at the distance larger than 10 D and thus is considered not adequate for the wake simulations. Further, the results from G1, G2, and G3 are very similar in the entire range. Therefore, as a compromise between accuracy and computational resources, the G2 grid was adopted for the simulations in this paper.

The velocity field of the wake in the *xOy* plane is shown in Fig. 16. It is shown that the wind velocity behind the wind turbine is reduced, and a shear layer is formed at the location of the blade tips. The reason for this phenomenon is that the wind turbine extracts the kinetic energy of the wind and transfers it to mechanical energy, which leads to the reduction of the wind velocity behind the

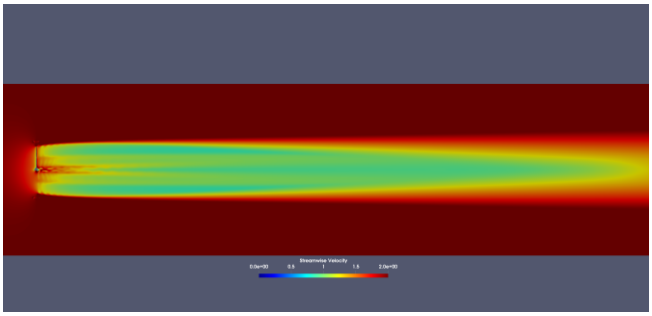

Fig. 16 Velocity field in the *xOy* plane

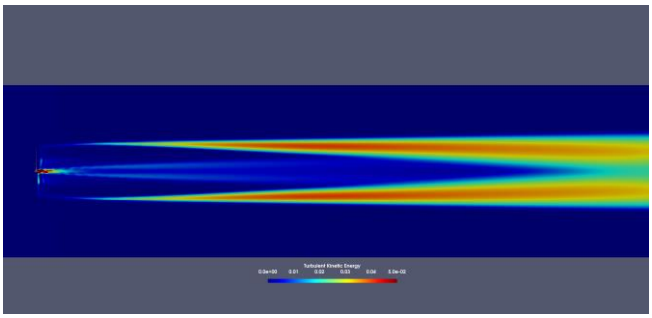

Fig. 17 Turbulent kinetic energy field in the *xOy* plane

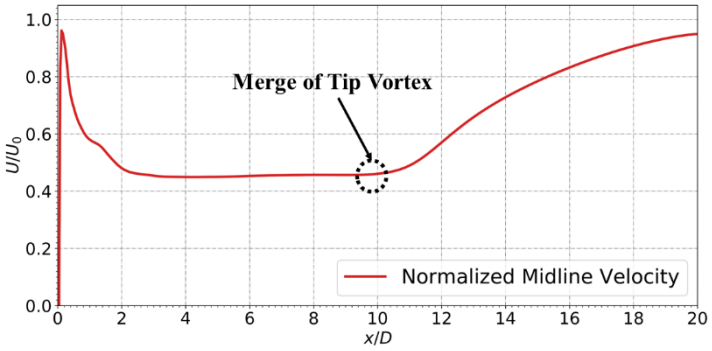

Fig. 18 Center-line velocity variation in the streamwise direction

rotor and an expansion of the wake. As a result, a velocity gradient in the radial direction around the location of the blade tips is formed and the shear layer is gradually thickening along the wake.

This can be better understood by looking at the turbulent kinetic energy field of the wake and the center-line velocity variation, as shown in Figs. 17 and 18. The width of the tip vortex is gradually expanding until it merges in the middle, as shown in Fig. 17. And this merge of the tip vortex brings momentum from the free-stream into the wake region and thus leads to the fast recovery of the center-line velocity, as shown in Fig. 18.

Finally, Fig. 19 presents the wake vortex structure of the turbine. Iso-surface of Q value (Hunt *et al.* 1988, Kamkar *et al*. 2010) equals 1 is visualized. The iso-surface is colored by velocity magnitude. In the figure, the blade tip vortex and the blade root/nacelle vortex are clearly resolved.

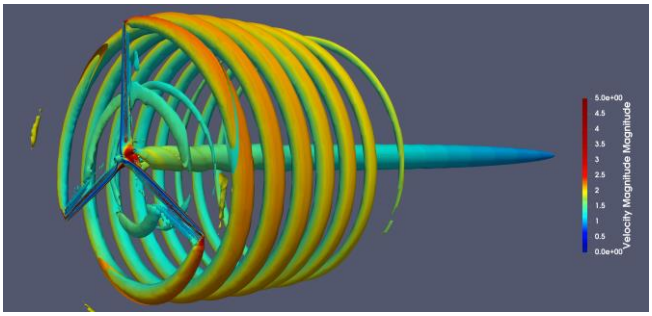

Fig. 19 Iso-surface of Q value equals 1 (colored by velocity magitude)

5. Conclusions

This study presents the results of CFD simulations of a model-scale wind turbine which was designed for wave tank experiments by using CFD code ReFRESCO. Steady-state simulations with the absolute formulation method (AFM) in ReFRESCO were carried out. The values of C_T and C_P of the turbine at different tip speed ratios (TSR) are obtained first. The results were compared against the experimental data and previous numerical results, and good agreement was achieved. Then, a systematic verification study with four different grids was performed for the performance of the turbine with respect to the grid resolution of the wake region. It was found that the grid resolution of the wake region does not affect the performance of the turbine significantly. Finally, the wake characteristics of the MSWT at TSR = 7 were presented and discussed. It was observed that the merge of the tip vortex enhanced the turbulence mixing in the wake region and lead to the fast recovery of the center-line velocity.

Acknowledgments

The authors would like to thank the High Performance Research Computing (HPRC) of Texas A&M University for providing the computational resources.

References

de Ridder, E.J., Otto, W., Zondervan, G.J., Huijs, F. and Vaz, G. (2014), "Development of a scaled-down floating wind turbine for offshore basin testing", *Proceedings of the ASME 2014 33rd International Conference on Ocean, Offshore and Arctic Engineering.* San Francisco, California, USA. June.

Duque, E.P.N., Van Dam, C.P. and Hughes, S.C. (1999), "Navier-Stokes Simulations of the NREL Combined Experiment Phase II Rotor", *37th Aerospace Sciences Meeting and Exhibit*, 143-153.

Eça, L. and Hoekstra, M. (2014), "A procedure for the estimation of the numerical uncertainty of CFD calculations based on grid refinement studies", *J. Comput. Phys.*, **262**, 104-130. https://doi.org/10.1016/j.jcp.2014.01.006.

Hexpress (2021), https://www.numeca.com/product/omnis-hexpress

Hunt, J.C.R., Wray, A.A. and Moin, P. (1988), "Eddies, Streams, and Convergence Zones in Turbulent Flows", *Proceedings of the 1988 Summer Program 1988*.

IEA (2019), "Offshore Wind Outlook 2019", International Energy Agency.

https://www.iea.org/reports/offshore-wind-outlook-2019

Jonkman, J., Butterfield, S., Musial, W. and Scott, G. (2009), "Definition of A 5-MW Reference Wind Turbine for Offshore System Development", Technical Report, NREL/TP-500-38060, NREL.

Klaij, C.M., Hoekstra, M. and Vaz, G. (2018), "Design, analysis and verification of a volume-of-fluid model with interface-capturing scheme," *Comput. Fluids*, **170**, 324-340. https://doi.org/10.1016/j.compfluid.2018.05.016

Li, Y., Paik, K., Xing, T. and Carrica, P.M. (2012), "Dynamic overset CFD simulations of wind turbine aerodynamics", *Renew. Energ.*, **37**, 285-298. https://doi.org/10.1016/j.renene.2011.06.029.

Lynch, C.E. and Smith, M.J. (2013), "Unstructured Overset Incompressible Computational Fluid Dynamics for Unsteady Wind Turbine Simulations", *Wind Energy*, **16**(7), 1033-1048. https://doi.org/10.1002/we.1532.

Make, M. and Vaz, G. (2015), "Analyzing scaling effects on offshore wind turbines using CFD," *Renew. Energ.*, **83**, 1326-1340. https://doi.org/10.1016/j.renene.2015.05.048.

Make, M., Vaz, G., Fernandes, G., Burmester, S. and Gueydon, S. (2015), "Analysis of aerodynamic performance of floating wind turbines using CFD and BEMT methods", *Proceedings of the 34th International Conference on Offshore Mechanics and Arctic Engineering*, St. John's, Newfoundland, Canada. May 31-June 5.

MARIN (2017), "ReFRESCO Theory Manual", Technical Report, MARIN – Maritime Research Institute Netherlands.

Martin, H.R., Kimball, R.W., Viselli, A.M. and Goupee, A.J. (2014), "Methodology for Wind/Wave Basin Testing of Floating Offshore Wind Turbines", *ASME. J. Offshore Mech. Arct. Eng.*, **136**(2). https://doi.org/10.1115/1.4025030.

Menter, F. R., Kuntz, M. and Langtry, R. (2003), "Ten years of industrial experience with the SST turbulence model", *Turbulence Heat Mass Transfer*, **4**(1), 625-632.

Office of Energy Efficiency & Renewable Energy (2021), Wind Turbines: the Bigger, the Better, Office of Energy Efficiency & Renewable Energy, DOE, https://www.energy.gov/eere/articles/wind-turbines-bigger-better

Pointwise (2022), https://www.pointwise.com

Roache, P.J. (2009). *Fundamentals of Verification and Validation*, Hermosa Publishers, Socorro, New Mexico, USA.

Kamkar, S.J., Jameson, A., Wissink, A.M. and Sankaran, V. (2010), "Feature-driven cartesian adaptive mesh refinement in the helios code", *Proceedings of the 48th AIAA Aerosciences Conference.*

Tran, T.T. and Kim, D. (2016), "A CFD study into the influence of unsteady aerodynamic interference on Wind turbine surge motion", *Renew. Energ.*, **90**, 204-228. https://doi.org/10.1016/j.renene.2015.12.013.

Troldborg, N. (2009), "Actuator Line Modeling of Wind Turbine Wakes," Technical University of Denmark, Denmark.

van Leer, B. (1974), "Towards the ultimate conservative difference scheme. II. Monotonicity and conservation combined in a second-order scheme", *J. Comput. Phys.*, **14**, 361-370. https://doi.org/10.1016/0021-9991(74)90019-9.

Veers, P., Dykes, K., Lantz, E., Barth, S., Bottasso, C.L., Carlson, O., Clifton, A., Green, J., Green, P., Holttinen, H., Laird, D., Lehtomäki, V., Lundquist, J.K., Manwell, J., Marquis, M., Meneveau, C., Moriarty, P., Munduate, X., Muskulus, M., Naughton, J., Pao, L., Paquette, J., Peinke, J., Robertson, A., Rodrigo, J. S., Sempreviva, A. M., Smith, J.C., Tuohy, A. and Wiser, R. (2019), "Grand challenges in the science of wind energy", *Science*, **366**(6464). https://doi.org/10.1126/science.aau2027.

Wang, Y., Chen, H.C., Koop, A. and Vaz, G. (2021), "Verification and validation of CFD simulations for semi-submersible floating offshore wind turbine under pitch free-decay motion", *Ocean Eng.*, **242**. https://doi.org/10.1016/j.oceaneng.2021.109993

Wind Energy Technologies Office (2021), Top 10 Things You Didn't Know About Offshore Wind Energy, Wind Energy Technologies Office, DOE, https://www.energy.gov/eere/wind/articles/top-10-things-you-didnt-know-about-offshore-wind-energy

Wu, Y. and Porté-Agel, F. (2015), "Modeling turbine wakes and power losses within a wind farm using LES: an application to the horns rev offshore wind farm", *Renew. Energ.*, **75**, 945-955.

https://doi.org/10.1016/j.renene.2014.06.019.
Xie, S. and Archer, C. (2017), "A numerical study of wind-turbine wakes for three atmospheric stability conditions", *Bound.-Lay. Meteorol.*, **165**(1), 87-112. https://doi.org/10.1007/s10546-017-0259-9.
Ye, M., Wang, Y., Chen, H.C., Koop, A., Rentschler, M. and Vital, Á.G. (2021), "CFD simulations of near and far wakes of two turbines in a tandem configuration", *Proceedings of the 31th (2021) International Ocean and Polar Engineering Conference*, Rhodes, Greece, June.
Ye, M., Chen, H.C. and Koop, A. (2022), "Comparison of Different Wind Turbine Modeling Strategies in CFD Simulations", *Proceedings of the 32th (2022) International Ocean and Polar Engineering Conference*, Shanghai, China, June.

MK